



Universiteit  
Leiden  
The Netherlands

## **Integrating cellular and tissue dynamics with cell fate decisions through computational modeling**

Heldring, M.M.

### **Citation**

Heldring, M. M. (2023, December 12). *Integrating cellular and tissue dynamics with cell fate decisions through computational modeling*. Retrieved from <https://hdl.handle.net/1887/3666239>

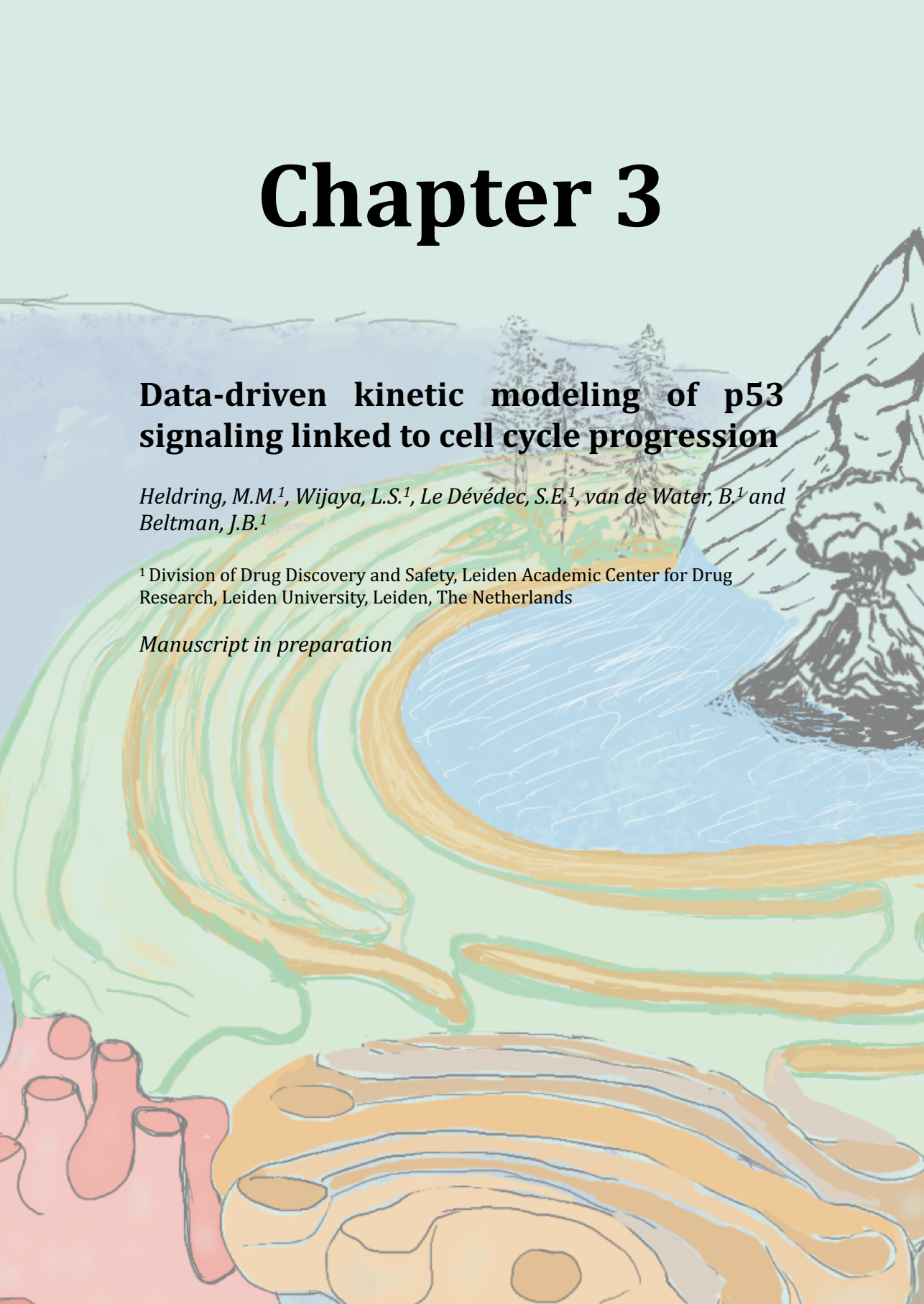
Version: Publisher's Version

License: [Licence agreement concerning inclusion of doctoral thesis in the Institutional Repository of the University of Leiden](#)

Downloaded from: <https://hdl.handle.net/1887/3666239>

**Note:** To cite this publication please use the final published version (if applicable).

# Chapter 3



## **Data-driven kinetic modeling of p53 signaling linked to cell cycle progression**

*Heldring, M.M.<sup>1</sup>, Wijaya, L.S.<sup>1</sup>, Le Dévédec, S.E.<sup>1</sup>, van de Water, B.<sup>1</sup> and Beltman, J.B.<sup>1</sup>*

<sup>1</sup>Division of Drug Discovery and Safety, Leiden Academic Center for Drug Research, Leiden University, Leiden, The Netherlands

*Manuscript in preparation*

## Abstract

Hepatocellular homeostasis is essential for maintaining a healthy and normal-functioning liver. Homeostatic disruption caused by chemical compounds can induce temporary or chronic liver injury and even complete liver failure. There is a vast array of proteins involved in cellular homeostasis that controls the response to diverse types of stress. Among the most important is the transcription factor p53, primarily known for its function to maintain genomic stability, regulate transient and permanent cell cycle arrest and apoptosis. Activated p53 transcriptionally regulates the expression of many proteins, among which are MDM2, p21 and BTG2. MDM2 functions as a direct inhibitor of p53 by targeting it for ubiquitination. The proteins p21 and BTG2 are known for their regulatory function in G1 and G2 cell cycle arrest. Using HepG2-FUCCI cells, we showed that exposure to cisplatin or etoposide caused a temporary G2 arrest. To study the link between protein expression and cell cycle arrest, we developed an ODE model in which we integrated a previously established model for the protein expression dynamics of p53, MDM2, p21 and BTG2 with a cell cycle model. This allowed us to determine the importance of p21 and BTG2 in their stimulation of G1 and G2 cell cycle arrest. We found that the protein dynamics could predict the G2 cell cycle arrest in cisplatin-treated cells, but not in cells exposed to etoposide. We show that assumptions of continued transition of phase G2 to G1 without mitosis as well as modified phase transition rates can explain the cell cycle data for low concentrations of etoposide, which suggests influence of proteins other than p21 and BTG2. In conclusion, we provide a basic model that can be extended with additional cell cycle regulators besides p21 and BTG2 to improve our quantitative understanding of cell cycle arrest.

## Introduction

The process of drug development is a time consuming and very costly exercise, in which more than 90% of the initial drug candidates fail due to safety concerns<sup>1</sup>. In the pre-clinical phase, tens to hundreds of drug candidates are screened on eliciting adverse effects<sup>1,2</sup>, for which animals are still widely used. However, animal testing to predict human toxicity is not as effective and reliable as often anticipated: preclinical tests in animal models are used to detect adverse effects, but almost 90% of the drug candidates that enter clinical trials fails<sup>3</sup>. To reduce the number of animals used for drug testing, development of alternatives such as *in silico* tools and *in vitro* experiments with human cells are necessary. With such methods, we can study the functioning and activation of protective stress response pathways upon exposure to chemicals and their role in the regulation of cell fate. Together with an understanding of how stress-affected cell fate relates to the functioning of tissues and organs, these methods can in the future be used to predict adverse effects in humans without the use of animal experiments.

Transcription factor p53 interferes with many stress response pathways, which makes it an important protein for the maintenance of cellular homeostasis and therefore a highly relevant protein to study in the context of drug safety. It is most known for its function as protector of the DNA, because it responds to DNA damage and transcriptionally regulates DNA-damage signal effectors that are involved in DNA repair, cell cycle arrest, and apoptosis. However, the processes that determine whether cells commit to cell cycle arrest or apoptosis are not fully understood. Several studies showed that the activity of p53 as a transcription factor and thereby differential regulation of the expression of genes involved in cell fate processes is dependent on p53 post-translational modifications (reviewed in <sup>4,5</sup>). In addition, the oligomeric state of p53, i.e., monomeric, dimeric or tetrameric p53 structures, affects the gene expression profile and consequent cell fate decisions <sup>6</sup>. Besides the form of p53 itself, the presence of cofactors is essential for the activation of several genes. For example, the cell cycle inhibitor p21 is only activated by p53 in the presence of p300 <sup>7</sup> and ASPP protein specifically enhances p53-dependent apoptosis, but not cell cycle arrest, by physically interacting with p53 <sup>8</sup>. Yet another factor that influences cell fate decisions is prior p53-mediated mitochondrial apoptotic priming, which promotes apoptosis in case of p53 reactivation <sup>9</sup>. Finally, the role of the temporal dynamics of p53 in cell fate determination has been extensively studied. Pulsatile p53 dynamics represent a protective mechanism that increases the likelihood of recovery <sup>10,11</sup>, whereas sustained, rapid p53 accumulation leads to cell death <sup>12</sup>. Thus, many factors influence the functionality of p53 and the expression of its downstream targets.

To understand the p53-dependent regulation of cell behavior, we clearly need to quantify how downstream target gene expression relates to cell fate. The cyclin-dependent kinase (CDK) inhibitor p21 is an important p53 downstream target and is mostly known for its role in cell cycle arrest. During the replicative cell cycle, proteins of the cyclin family drive the progression of one cell cycle phase to the next. In mammalian cells, this is regulated through the expression of the Cyclins C and D during G1 phase, Cyclin E during G1/S transition, Cyclin A during S and G2 phase and Cyclin B during mitosis <sup>13</sup>, and through subsequent binding and activation of these cyclins to their specific CDK binding partners. The complexes Cyclin D-CDK4/6 and Cyclin E-CDK1/2 are inhibited by p21, which causes G1 arrest <sup>13,14</sup>. However, G1 arrest is not solely dependent on p21. The p53-inducible protein BTG2 is also known for its antiproliferative function <sup>15</sup> and can promote G1 cell cycle arrest via downregulation of Cyclin D <sup>16</sup>. Moreover, p21 inhibits Cyclin A-CDK1/2 complexes and to a lesser extent Cyclin B/CDK1 <sup>17</sup>, whereas BTG2 is a more potent inhibitor of Cyclin B and can cause G2/M arrest and cell death <sup>18</sup>. These findings underline the importance of p21 and BTG2 as regulators of cell cycle progression, yet they do not yet reveal the relative importance of these effects on the cell cycle.

In this study, we therefore investigated the quantitative influence of p21 and BTG2 on cell cycle progression after p53 activation upon exposure to cisplatin (CDDP) and etoposide. To quantitatively describe the relation between p21/BTG2 expression and cell cycle, we used our previously established Ordinary Differential Equation (ODE) model for the DNA damage signaling pathway and coupled this to a simplified cell cycle progression model that simulates the number of cells in different cell cycle phases. We used HepG2 cells with a Fluorescent Ubiquitination-based Cell Cycle Indicator (FUCCI) construct in combination with live-cell confocal microscopy to measure the temporal dynamics of the number of cells in G1 and S-G2-M phases. These data showed that cisplatin-induced DNA damage causes a temporary cell cycle arrest in G2 with subsequent cell cycle continuation and mitosis, whereas cells arrested in G1 in control conditions. By subsequently calibrating our model to these data, we could quantify the importance of p21 and BTG2 in the regulation of cell cycle transitions. Specifically, we found that BTG2 was required to describe the G2 arrest in cisplatin-treated cells. Interestingly, the G2 arrest in cells treated with etoposide could not be explained by BTG2 or p21 expression, unless transition of phase G2 to G1 took place without mitosis and at a lower rate than in cisplatin-treated cells. This suggests that other regulatory factors than p21 and BTG2 are partially responsible for the etoposide-induced G2 arrest. Our model provides an excellent basis for the integration of protein dynamics with cell cycle progression and can be extended to further improve our understanding of cell cycle regulation in response to genotoxic and other forms of molecular stress.

## Methods

### Cell culture

Human hepatoma (HepG2) cells were purchased from ATCC – Germany (clone HB8065) and maintained in DMEM high glucose (Fisher Scientific – Bleiswijk, The Netherlands) supplemented with 10% (v/v) FBS (Fisher Scientific – Bleiswijk, The Netherlands), 250 U/ml penicillin and 25 µg/ml streptomycin (Fisher Scientific – Bleiswijk, The Netherlands) in humidified atmosphere at 37 degrees Celsius and 5% CO<sub>2</sub>/air mixture. We used the cells at a passage number lower than 20 and seeded in Greiner black µ-clear 96 well plates, at 32,000 cells per well for the exposure experiment.

### Stable FUCCI reporter cell line generation

We generated the HepG2-FUCCI reporter cell line using a lentiviral vector. The plasmid expressing the FUCCI reporter system was generously provided by Leiden University Medical Centrum in The Netherlands. We generated the lentivirus containing FUCCI plasmid in HEK293T cells cultured in the same medium as mentioned above. HEK293T cells were seeded in 6 cm dishes with a density of 400,000 cells per dish and reached 60-80% confluency after 24 h. For transfection 24 h after seeding, we prepared a mixture of the viral particle DNA composed of VSV (0.7 µg), GAG (1.3 µg), REV (1.0 µg) and the FUCCI-expressing

plasmid (2 µg) in 150 µl serum and antibiotic free medium. Next, we prepared a mixture of PEI (10 µl) in serum and antibiotic free medium (140 µl) and incubated it for 5 minutes at room temperature (RT). Hereafter, we slowly added the DNA mixture, followed by another 15 minutes incubation time. We added the mixture drop by drop to the HEK293T cells cultured in antibiotic free medium covering the culture surface area. After 24 h, we exchanged the medium with antibiotic free medium. We harvested the virus in the medium by collecting and passing the medium through a 0.45 µm sterile filter to eliminate the cell debris 48 h after the transfection. We performed transduction of the HepG2 cells that had grown in a 6 well plate to ~70% confluency. On the day of transduction, we replaced the medium of the cells with 1 ml of the medium containing lentivirus carrying the FUCCI construct and added 1 µl of polybrene to enhance the transduction efficiency. We replaced this medium with culture medium after 24 h of transduction. The HepG2-FUCCI cells were then allowed to proliferate to obtain sufficient cells for further experiments.

### Exposure and imaging

We exposed HepG2-FUCCI cells to chemicals two days after seeding on a 384 wells plate. We replaced the medium with medium containing Hoechst 33342 (1:10000 dilution) for nuclear staining 2 h before exposure. After 2 h of incubation with Hoechst, we replaced the medium with cisplatin-containing medium (Ebewe). Exposure of cells originating from three different flasks was done in triplicate on the same day and from the same plate. Directly after compound exposure, we transferred the plates to a Nikon TiE2000 confocal laser microscope (laser: 540 nm – for Cdt1 detection, 488 nm – for Geminin detection, and 408 nm – for Hoechst nuclear staining detection) equipped with automated stage and perfect focus system, and started imaging with a 20x magnification objective at two distinct positions per well for 72 h with one imaging round per 25 minutes. During imaging, the plates were maintained in humidified atmosphere at 37 degrees Celsius and 5% CO<sub>2</sub> /air mixture.

### Image and data analysis

Following image acquisition, we identified the nuclei in each image based on the Hoechst signal with the watershed masked clustering algorithm<sup>19</sup> in ImageJ. The segmentation images together with the confocal microscopy images for Hoechst, Geminin-GFP and Cdt1-RFP were loaded into CellProfiler version 3.1.9. To obtain the Geminin-GFP and Cdt1-RFP intensity per nucleus, we executed a pipeline that used the IdentifyPrimaryObjects and MeasureObjectIntensity modules and the in-house H5CellProfiler method<sup>20</sup> to convert the exported HDF5 files into a data matrix containing quantifications per single cell.

We performed various subsequent data analysis steps on the fluorescence mean intensities within segmented nuclei using R version 4.2.2. Because a small proportion of the Cdt1-RFP signal leaked into the Geminin-GFP emission spectrum, the Geminin-GFP mean intensities were consistently increased with a

proportion  $c$  of the Cdt1-RFP signal. We approximated  $c$  by obtaining the nucleus with the highest Cdt1-RFP/Geminin-GFP ratio and taking  $c$  as the ratio between the Geminin and Cdt1 expression for this nucleus. With the formula  $G_{corr} = G - c \cdot C$ , where  $G_{corr}$  is the corrected Geminin intensity,  $G$  the Geminin intensity and  $C$  the Cdt1 intensity, we corrected the Geminin-RFP expression. Based on the low expression of Cdt1 and Geminin at the start of imaging, we set the threshold for the intensity below which cells were considered Cdt1- or Geminin-negative at 5% of the maximum expression. Such ‘colorless’ cells were defined as early G1 or G0 phase cells. Cells with a Cdt1-RFP intensity higher than the threshold were classified as cells in G1 phase, whereas cells with a Cdt1-RFP intensity lower but Geminin-GFP intensity higher than the threshold were categorized as S-G2-M cells. Per measurement time point, we counted the number of cells in each phase and normalized these numbers by dividing them by the total number of cells per image at the start of imaging. We used the mean of the two technical replicates to obtain a single value for each biological replicate. For the purpose of fitting these measurements to the cell cycle ODE model (see below), we predicted the normalized number of cells in each phase category at fixed 1.5 h intervals, i.e., the same time intervals used for fitting the protein expression data in <sup>21</sup>, by fitting a polynomial spline using a B-spline basis matrix with degree 3 and 6 degrees of freedom.

The image-based protein expression data after etoposide exposure published in <sup>22</sup> was processed in a similar manner as we analyzed the data for cisplatin, which we explained in <sup>23</sup> and which we re-used here. In short, we used the protein expression data on single cell level and calculated the geometric mean of the GFP expression over all cells per image. Next, we calculated the average GFP value of the two technical replicates and performed background subtraction per plate and per time point by subtracting the average of the DMSO controls from the average in etoposide exposure conditions. Finally, we applied min-max normalization to obtain scaled GFP-intensity values between 0 and 1, and aligned the measurement time points of the different biological replicates with a B-spline function (df = 6, degree = 3) to obtain a readout every 1.5 h, starting at 1 and ending at 71.5 h. We used the readouts for propidium iodide-positive (PI<sup>+</sup>) and Annexin V-positive (AnV<sup>+</sup>) cells to calculate the fraction of dead cells. Specifically, we classified a cell as PI<sup>+</sup> or AnV<sup>+</sup> if the overlap between its nucleus and the AnV or PI fluorescent signal was more than 10% of the nuclear area.

### **Modeling**

We used the p53 signaling model in <sup>21</sup> to simulate p21 and BTG2 dynamics. In brief, phosphorylation of p53 triggered by cisplatin-induced DNA damage causes transcriptional activation of MDM2, p21 and BTG2, while MDM2 inhibits p53 and phosphorylated p53 (p53-p) (see Supplementary Methods). We built a simplified cell cycle model and integrated the p21 and BTG2 state variables to simulate the effect of p21 and BTG2 expression on cell cycle progression. In the cell cycle model, we distinguished four cell cycle phases, i.e., early G1, G0, G1 and

S-G2-M. At the start of the cycle, cells are in early G1 phase. Each cell can either progress in the cell cycle and enter G1 phase with rate  $r_{G1}$  or exit the cell cycle into quiescence (G0) with rate  $r_{exit}$ . From G0, cells can reenter the cell cycle in G1 phase with rate  $r_{entry}$ . Cells in G1 progress to S-G2-M phase with rate  $r_{SG2M}$  and subsequently divide with mitosis rate  $r_{mit}$ . Mitosis of a cell leads to the 'birth' of two daughter cells that are in early G1 phase. To explain the accumulation of G1 cells in control conditions, we included resources  $R$  as additional state variable. Resources, such as growth factors, nutrients and unoccupied space, stimulate the transition from G1 to S-G2-M, but are depleted with a rate depending on the total number of cells scaled with factor  $s$ . Modeling the effect of p21 and BTG2 on cell cycle progression required integration of these proteins in the cell cycle model. Because p21 and BTG2 are both known to play a role in G1 and G2 arrest, we made the transition rates from G1 to S-G2-M and from S-G2-M to early G1 phase dependent on these proteins. We achieved this by dividing the appropriate transition rates by the scaled and weighted amounts of p21 and BTG2, i.e.,  $P_1$  and  $P_2$ , where

$$P_1 = 1 + \left( k_1 (sf_{BTG2} \cdot BTG2 + offset_{BTG2}) + k_2 (sf_{p21} \cdot p21 + offset_{p21}) \right), \text{ and} \quad Eq. 1$$

$$P_2 = 1 + \left( k_3 (sf_{BTG2} \cdot BTG2 + offset_{BTG2}) + k_4 (sf_{p21} \cdot p21 + offset_{p21}) \right). \quad Eq. 2$$

Note that our previously published estimates for the scaling and offset parameters  $sf_{BTG2}$ ,  $sf_{p21}$ ,  $offset_{BTG2}$  and  $offset_{p21}$ <sup>21</sup> (Supplementary Table 1) were used to linearly transform the simulated BTG2 and p21 dynamics to match the data from<sup>23</sup>, whereas the parameters  $k_1$ ,  $k_2$ ,  $k_3$ , and  $k_4$  were required to scale the relative influence of p21 and BTG2 on the cell cycle transitions. The ODEs for the cell cycle model thus became:

$$\frac{dR}{dt} = - (G1_{early} + G0 + G1 + SG2M) \cdot s \cdot R, \quad Eq. 3$$

$$\frac{dG1_{early}}{dt} = \frac{2 \cdot r_{mit} \cdot SG2M}{P_1} - r_{exit} \cdot G1_{early} - r_{G1} \cdot G1_{early}, \quad Eq. 4$$

$$\frac{dG0}{dt} = r_{exit} \cdot G1_{early} - r_{entry} \cdot G0, \quad Eq. 5$$

$$\frac{dG1}{dt} = r_{entry} \cdot G0 + r_{G1} \cdot G1_{early} - \frac{r_{SG2M} \cdot G1 \cdot R}{P_2}, \text{ and} \quad Eq. 6$$

$$\frac{dSG2M}{dt} = \frac{r_{SG2M} \cdot G1 \cdot R}{P_2} - \frac{r_{mit} \cdot SG2M}{P_1}. \quad Eq. 7$$

We made small changes to this default model (M1) to explore the effect of different model components on the simulations. Specifically, to examine the influence of resources, we removed the dependency of the G1 to S-G2-M transition on  $R$  (M2). Moreover, we separately recalibrated the M1 model using the data until the 24 h time point (M3), to check whether this would improve the fit to data at early time points. To investigate the contribution of p21 and BTG2

to cell cycle progression, we alternately set  $k_i$  parameters to 0 (M4, M5 and M6). We used the best fit of the default model to examine whether p21 and BTG2 could fit the data for low etoposide exposure. For this purpose, we used the parameters from model M3, but re-estimated the  $k$ -parameters to fit the control data for etoposide exposure (M7). To simulate cell cycle progression without cell division, we removed the proliferation factor 2 in Equation 4. In addition, we manually changed the  $r_{mit}$ ,  $r_{G1}$ , and  $r_{SG2M}$  parameters to investigate whether modification of these parameters improved the simulations.

Calibration of all cell cycle models was done as described in <sup>23</sup>. In short, we used the sensitivity equations <sup>24</sup> to efficiently determine the path of steepest descent towards a local optimum. We performed optimization of the objective function with the least squares method of the SciPy package in Python version 3.7.3. To find the global optimum in the parameter space, we initialized the models 10 times with a parameter set retrieved by systematic sampling of the parameter space with Latin hypercube sampling <sup>25</sup>. The model fitting results with the lowest cost were considered the global optima. The parameter values used to simulate all models can be found in Supplementary Tables 1-4.

## Results

### HepG2 cells transiently arrest in G2 phase after cisplatin exposure

To study the effect of DNA damage-inflicted p53 activation on the cell cycle, we generated HepG2-FUCCI cells. These cells contain red fluorescent protein-labelled Cdt1 (Cdt1-RFP) and green fluorescent protein-labelled Geminin (Geminin-GFP) and therefore display a red or green color depending on the expression of Cdt1 and Geminin (Fig. 1A and 1B). During G1 phase, Cdt1 protein levels increase, whereas Geminin remains absent, which manifests as red colored cells. Cdt1 is degraded under influence of Geminin, which builds up during the transition from G1 to S phase. The presence of both Cdt1 and Geminin therefore briefly yields cells with a yellow color. In S, G2 and M phase, cells color green due to high Geminin expression. However, after mitosis Geminin is quickly degraded which renders the cells colorless. We measured the intensity of the RFP and GFP signals in HepG2-FUCCI cells with confocal microscopy (Fig. 1B) to obtain the distribution of cells per cell cycle phase over time. Cells were either left untreated, i.e., in presence of DMEM, or exposed to cisplatin just before imaging. As expected, because we did not aim to experimentally synchronize the cells, the cells were in different phases at the start of imaging (Fig. 1C, left images). Most cells were colorless (i.e., no red or green signal) at 0 h and only gained color over time, after entering the cell cycle (Fig. 1C). In addition, the images clearly showed that cell cycle progression is influenced by the exposure to cisplatin.

To determine the cell cycle phase per cell at every measurement time point, we used the Cdt1-RFP and Geminin-GFP expression intensity. We noticed that cells

with a high RFP intensity always transmitted some GFP signal as well, whereas cells with a high GFP intensity did not necessarily also transmit an RFP signal (Supplementary Figure 1A). Because there is some overlap between the emission spectra of GFP and RFP, the co-occurrence of GFP in RFP-positive cells was likely due to spectral leakage. We corrected for this minor effect by applying a scaling factor to the GFP intensity based on the Cdt1 intensity (Supplementary Figure 1B). Based on the RFP and corrected GFP intensities, we determined a threshold below which cells were considered colorless (i.e., no RFP or GFP expression). Because most cells had visually very low RFP and GFP expression at the start of imaging (Fig. 1C and Supplementary Figure 1C), we chose the

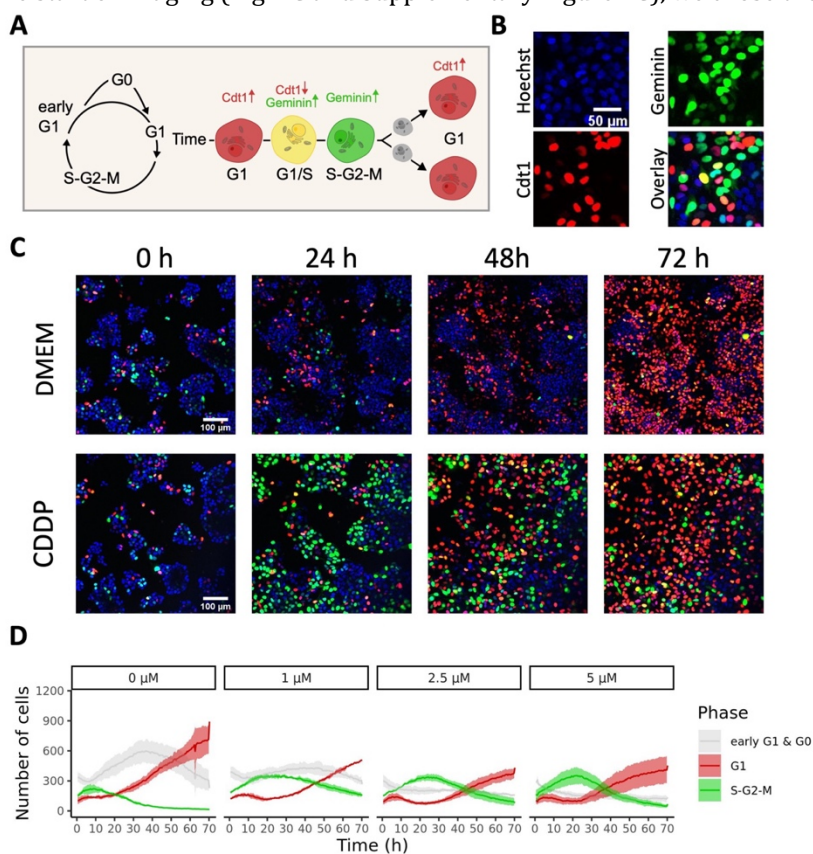


**Figure 1. Cisplatin induces transient G2 cell cycle arrest.** (A) Schematic overview of fluorescent signals during cell cycle progression in FUCCI HepG2 cells. Cells are red if Cdt1-RFP is present and green if Geminin-GFP is expressed. Yellow cells with both Cdt1 and Geminin expression are in a transition phase between G1 and S. Right after mitosis, cells are colorless (indicated with grey). (B) Example confocal microscopy images of HepG2 nuclei with Hoechst (blue), Cdt1 (red) and Geminin (green) fluorescent signals and their overlay. If both Cdt1 and Geminin are expressed, nuclei have a yellow color. (C) Example images of fluorescence in HepG2-FUCCI cells in control, medium (DMEM) condition and after 5  $\mu\text{M}$  cisplatin (CDDP) exposure. (D) Dynamics of the mean number of cells (solid lines) and standard deviation (shaded areas) in early G1 and G0, G1, and S-G2-M cell cycle phases at different cisplatin exposure concentrations.

threshold such that most cells were classified as colorless at 0 h. These cells were presumably residing in a quiescent G0 phase at 0 h and entered the cell cycle during imaging, or these cells may have just undergone mitosis and therefore were in the colorless early G1 phase. Cells with a Cdt1 expression higher than the threshold were considered to reside in G1 phase, whereas cells with a Cdt1-RFP expression lower but a Geminin-GFP expression higher than the threshold were classified as S-G2-M phase cells (Supplementary Figure 1D). Based on this classification scheme, we estimated the number of cells in each cell cycle phase over time (Fig. 1D). This analysis showed that in control conditions HepG2 cells rapidly arrested in G1, in most cases presumably after one cell division. In contrast, cells that were exposed to cisplatin first went through a temporary G2 arrest, indicated by the accumulation of cells in S-G2-M phase around 24 h, prior to a halt in G1 phase at 72 h. This effect was stronger for high than for low cisplatin concentrations, which was also illustrated by a slow cell population growth at high concentrations (Supplementary Figure 2). In conclusion, cisplatin-induced DNA damage leads to a transient G2 arrest in HepG2 cells.

### **Limitation of resources drives G1 arrest in control conditions**

Because p21 and BTG2 are both known to play a role in cell cycle arrest, we examined the relative contribution of these proteins to changes in the cell cycle. For this purpose, we quantified the effect of these proteins on cell cycle progression by expanding our previously established ODE model<sup>21</sup> with a cell cycle model (Fig. 2A). In this model, cisplatin causes DNA damage that leads to phosphorylation of p53 (p53-p). Active, phosphorylated p53 transcriptionally activates p21 and BTG2 in addition to MDM2, a protein that negatively regulates p53. Simulation of this model shows the dependency of MDM2, p21 and BTG2 expression on p53 activation (Supplementary Figure 3A). We connected this model to a simplified cell cycle model that simulates the number of cells in G1 early, G0, G1 and S-G2-M phases with parameters that describe the transition rates between phases. The temporal expression dynamics of p21 and BTG2 were considered to jointly inhibit the transition from G1 to S-G2-M phase and the S-G2-M to G1 early transition (Fig. 2A). In addition, we included a fifth state variable in the model that described the availability of resources such as growth factors, nutrients and free space, and that also affected the transition from G1 to S-G2-M phase.

Model parameter calibration to the experimental data generated an excellent fit in control conditions (Fig. 2B). Specifically, in the optimal model solution, cells exited the G0 phase at the start of the simulation and entered the cell cycle (Supplementary Figure 3B). Most cells remained arrested in G1 phase directly after entering the cell cycle or after one cell division, indicated by the stalling of proliferation around 50 h before the population had doubled (Supplementary Figure 2). The model predicted that resources were largely depleted around 30 h (Supplementary Figure 3C). Importantly, omission of the effect of resources led to a poor fit, both in control conditions and after cisplatin exposure, and

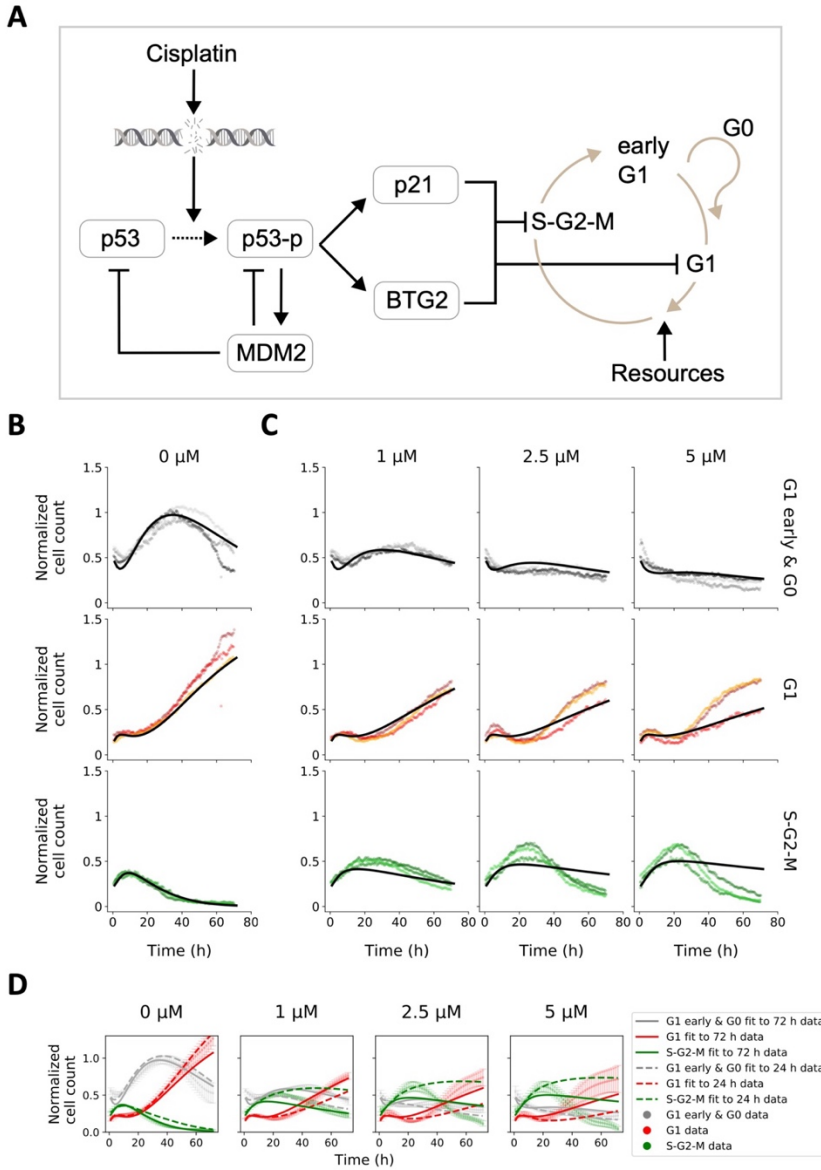


**Figure 2. BTG2 and p21 expression largely predicts cisplatin-induced transient G2 arrest followed by G1 arrest.** (A) Illustration of the structure of our ODE model, with p21 and BTG2 that can inhibit cell cycle progression in G1 and S-G2-M phase. (B-C) Model simulations (M1, black solid lines) after parameter estimation and the normalized experimental data in control conditions (B) and after cisplatin exposure (C). Data points of different colors represent the three independent biological replicates. (D) Comparison between the model fit in (B) and (C) for which all data points were used (M1), and a model fit for which only the data from 0-24 h (M3) was used for fitting. Data points represent the mean  $\pm$  sd of the three biological replicates.

could not fully explain the accumulation of cells in G1 phase in control conditions (Supplementary Figure 4). Thus, exhaustion of nutrients renders a plausible explanation for the observed G1 arrest in the control situation.

### **BTG2 is solely responsible for S-G2-M arrest upon cisplatin exposure**

Although the data from the exposure conditions at early time points could be well described with our model, the simulations only qualitatively reproduced the decrease in S-G2-M phase cells after 24 h and slightly underestimated the number of cells in G1 at late time points (Fig. 2C). The predictions for the S-G2-M arrest for the first 24 h could be further improved by using only that part of the data for model calibration (Fig. 2D). However, progression into mitosis and early G1 phase from the S-G2-M arrest could still not be fully explained.

Examination of the parameter estimates suggested that only p21 influenced the G1 to S-G2-M transition (see Supplementary Table 2, Model M1). However, simulation results were quite similar when we made the inhibition of the G1 to S-G2-M transition solely dependent on BTG2 by fixing  $k_4$  to zero (Fig. 3A) or when we completely removed the dependency of G1 to S-G2-M transition on the proteins (Fig. 3B). This suggests that the limited resources might in fact be the main driver for the G1 arrest at 72 h.

Further inspection of the estimated parameter values showed that BTG2 was responsible for the S-G2-M phase arrest upon cisplatin exposure (Supplementary Table 2, Model M1). Indeed, if we made the S-G2-M to G1 early transition solely dependent on p21 by fixing  $k_1$  to zero, the fit worsened, especially for the number of S-G2-M cells (Fig. 3C). Cells continued cycling after the transient S-G2-M arrest, yet the model simulations predicted a longer arrest (Fig. 2B) due to the continued high expression of BTG2 until 72 h (Fig. 2C). This suggests that other factors are forcing cell cycle progression, irrespective of continued high BTG2 expression that inhibits this progression.

### **BTG2 and p21 dynamics are insufficient to explain cell cycling upon etoposide treatment**

We next aimed to test whether the role of BTG2 in S-G2-M cell cycle arrest extends to similar DNA damaging compounds. Therefore, we examined whether an S-G2-M arrest caused by HepG2 cell exposure to the DNA topoisomerase II inhibitor etoposide, which prevents ligation of DNA double-strand breaks during S and G2 phase<sup>26</sup> and also leads to p21 and BTG2 induction<sup>22</sup>, could be explained with BTG2 induction. For this purpose, we recalibrated our p53 signaling model to data on protein expression after etoposide exposure (Fig. 4A) and again investigated to what extent BTG2 and p21 contributed to the changes in cell cycle progression after various etoposide exposure concentrations. Low etoposide concentrations, i.e., 0.5 and 1  $\mu\text{M}$ , caused a transient S-G2-M arrest (Fig. 4B) as was the case for cisplatin. In contrast to the S-G2-M arrest that

became more prominent with increasing cisplatin concentrations, at high etoposide concentrations (i.e., 5 and 10  $\mu\text{M}$ ) cells quickly bypassed the G2-M checkpoint and continued to G1 phase, indicated by the rapid drop of cells in S-G2-M phase (Fig. 4B).

To examine whether our model could describe these cell cycle progression data, we first recalibrated the k-parameters of the cell cycle model to the control data as these quantitatively somewhat differed for cisplatin and etoposide exposure (Fig. 4C). With this model we could not generate a good prediction of the observed S-G2-M cell cycle arrest at low etoposide concentrations, nor of the early G1 arrest at high concentrations (Supplementary Figure 5). We noticed that the p21 and BTG2 expression at low etoposide concentrations was only slightly higher than the basal expression in control conditions (Supplementary Figure 6A) and low in comparison to the cisplatin data, whereas the arrest in S-G2-M phase after etoposide exposure was more pronounced than in cisplatin-treated cells. Therefore, the rapid S-G2-M arrest that occurred in HepG2 cells exposed to low concentrations of etoposide is likely promoted by factors other than p21 and BTG2. Interestingly, we noticed that proliferation was greatly

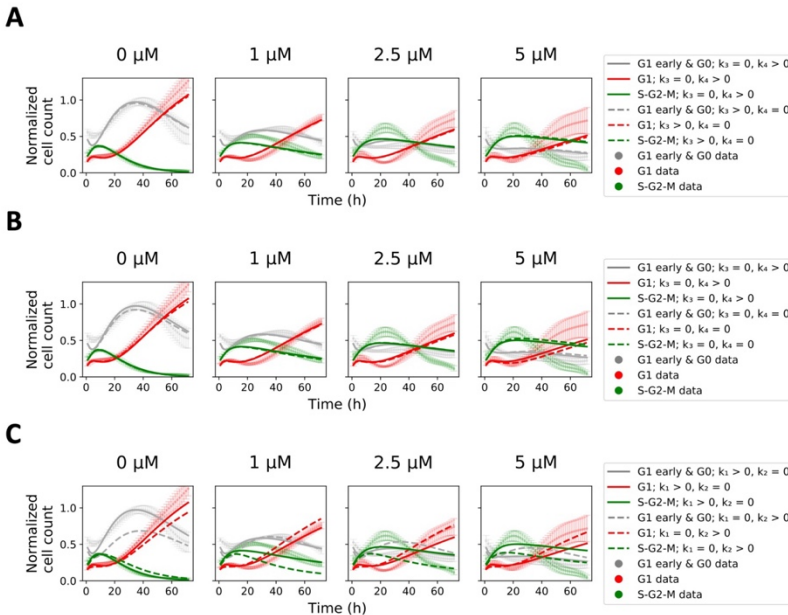


**Figure 3. Relative contribution of BTG2 and p21 to cell cycle arrest after cisplatin exposure.** (A) Simulations with solely p21 ( $k_3$  fitted close to 0, M1, solid lines) or solely BTG2 ( $k_4 = 0$ , M4, dashed lines) inhibiting G1 transition into S-G2-M phase in comparison to experimental data. (B) Simulations with ( $k_4 > 0$ , M1, solid lines) or without ( $k_4 = 0$ , M5, dashed lines) the influence of BTG2 on G1 transition into S-G2-M phase in comparison to experimental data. (C) Simulations with solely BTG2 ( $k_2$  fitted close to 0, M1, solid lines) or solely p21 ( $k_1 = 0$ , M6, dashed lines) inhibiting S-G2-M progression into mitosis in comparison to experimental data. Data points show mean  $\pm$  sd of three biological replicates.

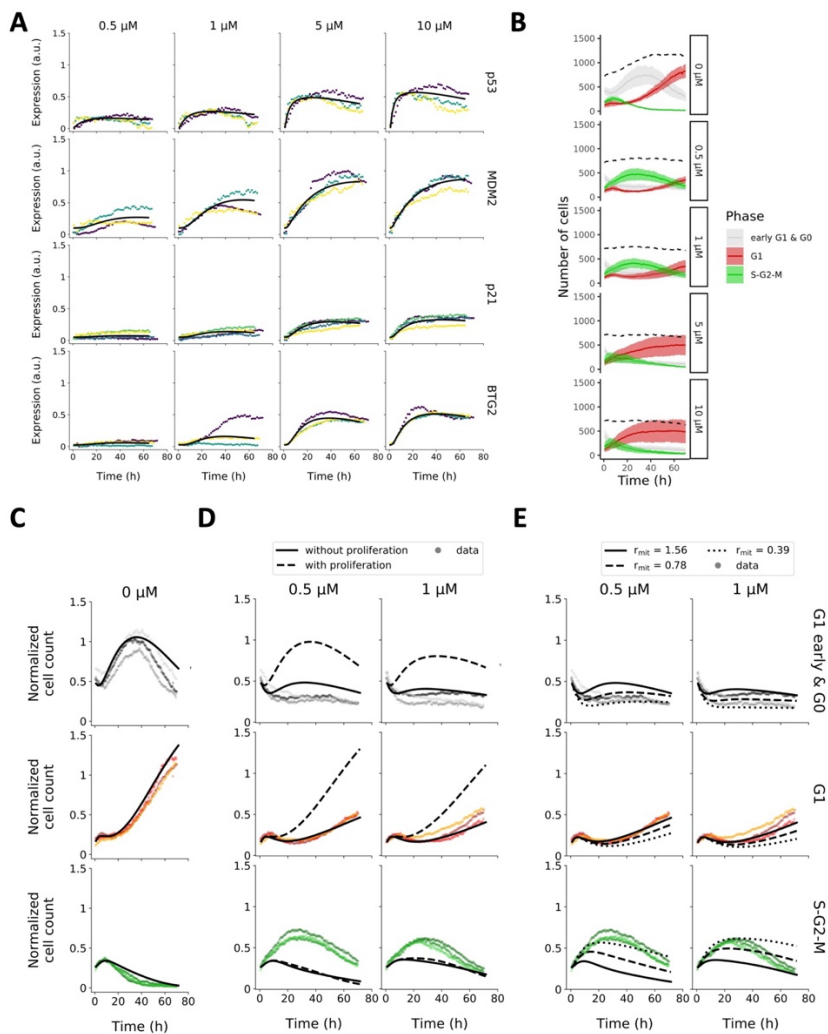


**Figure 4. BTG2 and p21 dynamics is insufficient to predict cell cycle progression in HepG2 cells after etoposide exposure.** (A) Simulation of DNA damage response proteins of the p53 signaling model after treatment with 0.5, 1, 5 and 10  $\mu\text{M}$  etoposide. (B) Dynamics of the mean number of cells (solid lines) and standard deviation (shaded areas) in early G1 and G0, G1, and S-G2-M cell cycle phases at different etoposide exposure concentrations. Dashed line indicates the total number of cells. (C) Fit of the cell cycle model (M7) with re-estimated  $k$ -parameters to the cell cycle data in control situation. (D-E) Simulation of the cell cycle model in (C) to the cell cycle data in low (0.5 and 1  $\mu\text{M}$ ) etoposide exposure conditions with cell cycle phase transitions, either with (dashed line) or without (solid line) cell division in (D), and without cell division and with modulation of the transition rate of S-G2-M to early G1 in (E). a.u., arbitrary units.

impaired already at 0.5  $\mu\text{M}$  etoposide, which was clear from the lack of growth of the cell population as a whole (Fig. 4B, dashed line) in combination with an

absence of cell death (Supplementary Figure 6B). Still, the decrease of cells in S-G2-M and increase of cells in G1 phase at late stages implied that cells were cycling. Because cells exposed to etoposide can undergo nuclear mis-segregation, or DNA replication and progression to G1 without mitosis, a process known as endocycling<sup>29</sup>, we questioned whether failed mitosis with continued cell cycle transition could be the reason for the decrease of cells in S-G2-M phase without an increase in population size. For this purpose, we removed the proliferation factor 2 in the equation that describes the transition from S-G2-M to G1 phase. This model adaptation improved the fit to the low-concentration etoposide data considerably, although the number of cells in S-G2-M arrest was still highly underestimated (Fig. 4D). In high exposure conditions, failed mitosis did not significantly improve the fit (Supplementary Figure 7A).

Finally, we hypothesized that a protein other than p21 or BTG2 might be responsible for the S-G2-M arrest after etoposide exposure in low exposure conditions. To test this hypothesis, we also lowered the mitosis rate ( $r_{mit}$ ) with a factor 2 and 4, which further improved the description of the data (Fig. 4E), although the number of cells in G1 phase was now slightly underestimated at late time points (Fig. 4E, dotted line). Similarly, modifications of the early G1 to G1 ( $r_{G1}$ ), G1 to S-G2-M ( $r_{SG2M}$ ) and S-G2-M to early G1 ( $r_{mit}$ ) transition rates improved the fit for the high etoposide concentrations (Supplementary Figure 7B). Our results show that the effect of etoposide on cell cycle progression is highly dependent on its concentration and that solely considering expression of proteins p21 and BTG2 to explain cell fate is not always sufficient.

## Discussion

Cell cycle progression is a complex cellular mechanism that involves numerous regulatory proteins. Externally induced cellular stress such as chemical-induced DNA damage can disrupt normal cell proliferation through the activation of proteins that interact with cyclins and CDKs, the drivers of cell cycle progression. Although the DNA damage signal effectors p21 and BTG2 can both be involved in inhibition of cell cycle progression during G1 and G2 cell cycle phases, their quantitative contribution to cell cycle arrest remains unknown. Our modeling approach showed that BTG2 could explain the G2 arrest induced by cisplatin exposure, but not the etoposide-induced G2 arrest. Indeed, p21 and BTG2 were only slightly induced by 0.5  $\mu\text{M}$  etoposide exposure compared to the control situation, while this low etoposide concentration already caused cells to arrest in G2 phase. In addition, cells appeared to progress into mitosis and G1 phase after a G2 arrest, even though p21 and BTG2 expression was persistently high. Thus, cell cycle arrest caused by chemically-induced DNA damage cannot be universally explained by the expression patterns of p21 and BTG2 alone, which underlines the necessity to include additional drivers of cell cycle arrest (or progression) to predict the effect of DNA damage on the cell cycle.

Cellular exposure to cisplatin and etoposide both caused an initial G2 arrest in our HepG2-FUCCI cells. Our model suggested that BTG2 and not p21 was involved in the cisplatin-induced G2 arrest. Indeed, disruption of BTG2 interferes with G2 arrest<sup>15</sup>, which indicates that BTG2 could be responsible for the cisplatin-induced G2 arrest. In contrast, p21 and BTG2 expression barely increased at 0.5  $\mu\text{M}$  etoposide exposure, whereas there was a profound accumulation of cells in S-G2-M phase. Our analysis showed that solely p21 and BTG2 expression was not sufficient to explain this etoposide-induced G2 arrest. Unlike a G1 arrest that is fully dependent on p53<sup>30</sup>, G2 arrest can occur in a p53-dependent and p53-independent manner<sup>28,30-32</sup>. Moreover, whereas BTG2 can induce a G2 arrest<sup>15</sup>, p21 seems mostly involved in the long-term maintenance of G2 arrest<sup>33,34</sup>. Thus, perhaps the DNA damage sensor proteins ATM, ATR, Chk1 and Chk2 that activate p53 signaling elicited a p53-independent onset of G2 arrest<sup>35-37</sup> after 0.5  $\mu\text{M}$  etoposide exposure, whereas the late and weak induction of p53-regulated protein p21 merely helped to sustain the G2 arrest. The possibility that different mechanisms establish the cisplatin- and etoposide-induced G2 arrests, indicates that the exact type of DNA damage influences the cellular response. In contrast to cisplatin that causes inter- and intrastrand crosslinks which activates p53 via ATR, Chk1 and Chk2<sup>38-41</sup>, etoposide exposure generates double-strand breaks that lead to p53 activation via ATM and Chk2<sup>35,42</sup>. Although both compounds induce p53 activation and (concentration-dependent) transient G2 arrest, the underlying molecular signaling cascade is different and therefore results in G2 arrest via different routes. With our work, we show that solely using the p53 downstream targets p21 and BTG2 to predict a DNA damage-induced G2 arrest is not always sufficient. Incorporation of proteins upstream of p53 in experimental studies and the model will contribute to reliable predictions of cell cycle arrest.

Because of the sustained expression of p53 and its downstream targets at late time points, the apparent continuation into mitosis and G1 arrest after the G2 arrest in both exposure conditions surprised us. Cell cycle progression after G2 arrest was especially evident for cisplatin-treated cells and cells exposed to low (0.5 and 1  $\mu\text{M}$ ) etoposide concentrations. In contrast, high (5 and 10  $\mu\text{M}$ ) etoposide concentrations immediately induced a G1 arrest, which puzzled us because etoposide affects the topoisomerase II enzyme, which is only active during S and G2 phase. This same phenomenon has been previously observed in normal murine mammary gland (NMuMG) cells. NMuMG cells went into a transient G2 cell cycle arrest at 1  $\mu\text{M}$  etoposide exposure, but directly into an apparent G1 arrest after exposure to 10  $\mu\text{M}$  etoposide<sup>29</sup>. Close examination showed that the cells exposed to 1  $\mu\text{M}$  etoposide failed mitosis due to nuclear mis-segregation. In addition, cells exposed to 10  $\mu\text{M}$  etoposide underwent endoreduplication, a process in which cells replicate the genome but bypass mitosis which leads to polyploidy. This also occurred in cisplatin-treated PROb colon carcinoma<sup>43</sup> and Chinese hamster ovary AA8 cells<sup>44</sup>. Although the observed accumulation of red HepG2 cells in our data could also mean that cells

adapt and enter mitosis despite damaged DNA<sup>45-48</sup>, the total number of cells barely increased, pointing to a lack of proliferation. Therefore, we hypothesized that HepG2 cells undergo nuclear mis-segregation or endoreplication instead of progressing into mitosis. Consistently, modification of the model by omitting proliferation while keeping cell cycle progression from S-G2-M to G1 phase improved the model fit for low etoposide concentrations. This suggests that etoposide prevents successful proliferation in HepG2 cells, although the factors responsible for this process remain to be identified. Lowering the mitosis rate further improved the fit, which implies that besides failed mitosis, other proteins than p21 and BTG2 could impact the phase transition rates and subsequent initiation of a G1 arrest. The improved fit for high etoposide exposure conditions by the transition rate parameter alterations strengthens this hypothesis. Indeed, the DDR is highly complex with 605 associated proteins that can be organized in multiple assemblies with distinct functions<sup>48</sup>. Possibly, proteins linked to other stress response pathways than the p53 signaling pathway play a role in this process. The central regulator of the oxidative stress response pathway NRF2 as well as its downstream targets are mildly activated upon etoposide exposure<sup>22,49</sup>. Because NRF2 can inhibit Cyclin D1 via activation of cyclin inhibitors p15, p21 and p27<sup>50</sup>, activation of this transcription factor could play a role in the fast G1 arrest at high etoposide concentrations. Yet, we do not have information on the expression of other cyclin inhibitors than p21. Besides such data, additional experiments with DNA damaging stressors that induce a direct G1 arrest would be helpful.

We aimed to predict cell cycle behavior based on the average p21 and BTG2 expression of a population of cells. Although our HepG2 cells are genetically almost identical, the cells varied in the expression of proteins, and cell cycles were not synchronized. Such variability can exert their effect on the cell cycle of individual cells in various ways: differences in the time dynamics and extent of p53 expression determine whether a cell initiates cell cycle arrest or apoptosis<sup>12</sup>. Similarly, basal p21 expression controls quiescence or cell cycle entry<sup>51</sup>, whereas p21 dynamics determine whether a cell remains in a proliferative state or becomes senescent<sup>52</sup>. In addition, cells respond differently to genomic stress depending on the cell cycle stage<sup>53</sup>. Other factors such as the microenvironment<sup>54,55</sup> and general stochasticity<sup>56</sup> can cause heterogeneity in the behavior of individual cells. Thus, although a study into the relation between protein dynamics and cell fate on population level can generate useful insights, single cell data can further elucidate the mechanistic regulation of cell cycle progression after genotoxic stress.

Integrating protein dynamics and cell cycle progression in one model is a useful approach to unravel the effect of low-level molecular interactions on a high-level process such as cell fate. Even though p21 and BTG2 are both well-known regulators of the cell cycle, we showed that their expression dynamics are not always sufficient to predict cell cycle arrest and continuation following

genotoxic stress. In addition to the inclusion of p53 downstream targets, extension of the model with the activation dynamics of kinases upstream from p53 could improve its predictive capacity. This will help to elucidate the quantitative mechanisms behind cell cycle regulation and predict adverse effects of chemicals in an early stage of drug safety testing.

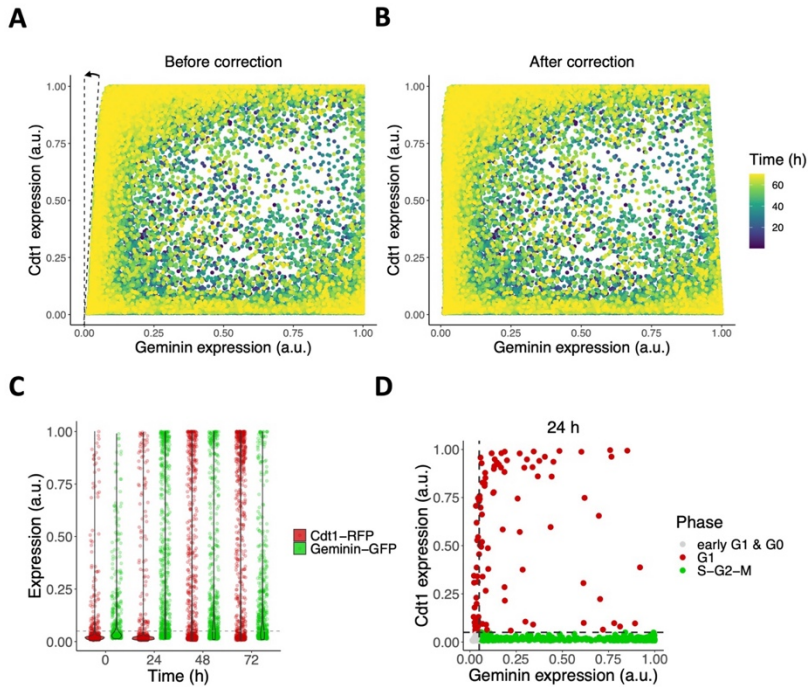
## References

1. Sun, D., Gao, W., Hu, H. & Zhou, S. Why 90% of clinical drug development fails and how to improve it? *Acta Pharm Sin B* **12**, 3049–3062 (2022).
2. Matthews, H., Hanison, J. & Nirmalan, N. “Omics”-Informed Drug and Biomarker Discovery: Opportunities, Challenges and Future Perspectives. *Proteomes* **4**, (2016).
3. Van Norman Gail A. Limitations of Animal Studies for Predicting Toxicity in Clinical Trials. *JACC: Basic to Translational Science* **4**, 845–854 (2019).
4. Laptenko, O., Tong, D. R., Manfredi, J. & Prives, C. The Tail That Wags the Dog: How the Disordered C-Terminal Domain Controls the Transcriptional Activities of the p53 Tumor-Suppressor Protein. *Trends Biochem. Sci.* **41**, 1022–1034 (2016).
5. Hafner, A., Bulyk, M. L., Jambhekar, A. & Lahav, G. The multiple mechanisms that regulate p53 activity and cell fate. *Nat. Rev. Mol. Cell Biol.* **20**, 199–210 (2019).
6. Fischer, N. W., Prodeus, A., Malkin, D. & Gariépy, J. p53 oligomerization status modulates cell fate decisions between growth, arrest and apoptosis. *Cell Cycle* **15**, 3210–3219 (2016).
7. Espinosa, J. M. & Emerson, B. M. Transcriptional regulation by p53 through intrinsic DNA/chromatin binding and site-directed cofactor recruitment. *Mol. Cell* **8**, 57–69 (2001).
8. Samuels-Lev, Y. *et al.* ASPP proteins specifically stimulate the apoptotic function of p53. *Mol. Cell* **8**, 781–794 (2001).
9. Sánchez-Rivera, F. J. *et al.* Mitochondrial apoptotic priming is a key determinant of cell fate upon p53 restoration. *Proc. Natl. Acad. Sci. U. S. A.* **118**, (2021).
10. Chen, X. *et al.* DNA damage strength modulates a bimodal switch of p53 dynamics for cell-fate control. *BMC Biol.* **11**, 73 (2013).
11. Purvis, J. E. *et al.* p53 dynamics control cell fate. *Science* **336**, 1440–1444 (2012).
12. Paek, A. L., Liu, J. C., Loewer, A., Forrester, W. C. & Lahav, G. Cell-to-Cell Variation in p53 Dynamics Leads to Fractional Killing. *Cell* **165**, 631–642 (2016).
13. Martínez-Alonso, D. & Malumbres, M. Mammalian cell cycle cyclins. *Semin. Cell Dev. Biol.* **107**, 28–35 (2020).
14. Harper, J. W., Adami, G. R., Wei, N., Keyomarsi, K. & Elledge, S. J. The p21 Cdk-interacting protein Cip1 is a potent inhibitor of G1 cyclin-dependent kinases. *Cell* **75**, 805–816 (1993).
15. Rouault, J. P. *et al.* Identification of BTG2, an antiproliferative p53-dependent component of the DNA damage cellular response pathway. *Nat. Genet.* **14**, 482–486 (1996).
16. Guardavaccaro, D. *et al.* Arrest of G(1)-S progression by the p53-inducible gene PC3 is Rb dependent and relies on the inhibition of cyclin D1 transcription. *Mol. Cell Biol.* **20**, 1797–1815 (2000).
17. Harper, J. W. *et al.* Inhibition of cyclin-dependent kinases by p21. *Mol. Biol. Cell* **6**, 387–400 (1995).
18. Ryu, M. S. *et al.* TIS21/BTG2/PC3 is expressed through PKC-delta pathway and inhibits binding of cyclin B1-Cdc2 and its activity, independent of p53 expression. *Exp. Cell Res.* **299**, 159–170 (2004).
19. Yan, K. & Verbeek, F. J. Segmentation for High-Throughput Image Analysis: Watershed Masked Clustering. in *Leveraging Applications of Formal Methods, Verification and Validation. Applications and Case Studies* 25–41 (Springer Berlin Heidelberg, 2012).
20. Wink, S., Burger, G. A., Le Dévédec, S. E., Beltman, J. B. & van de Water, B. User-friendly high-content imaging analysis on a single desktop: R package H5CellProfiler. *bioRxiv* 2022.10.06.511212 (2022) doi:10.1101/2022.10.06.511212.
21. Heldring, M. M., Shaw, A. H. & Beltman, J. B. Unraveling the effect of intra- and intercellular processes on acetaminophen-induced liver injury. *NPJ Syst Biol Appl* **8**, 27 (2022).

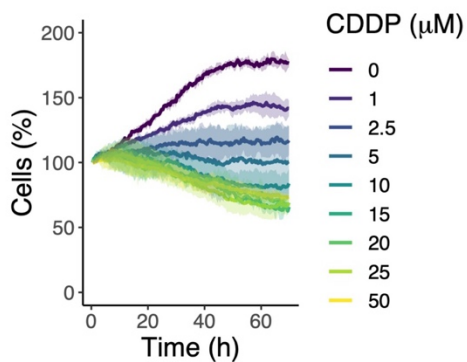
22. Wijaya, L. S. *et al.* Integration of temporal single cell cellular stress response activity with Logic-ODE modeling reveals activation of ATF4-CHOP axis as a critical predictor of drug-induced liver injury. *Biochem. Pharmacol.* 114591 (2021).
23. Heldring, M. M. *et al.* Model-based translation of DNA damage signaling dynamics across cell types. *PLoS Comput. Biol.* **18**, e1010264 (2022).
24. Raue, A. *et al.* Lessons learned from quantitative dynamical modeling in systems biology. *PLoS One* **8**, e74335 (2013).
25. Owen, A. B. A Central Limit Theorem for Latin Hypercube Sampling. *J. R. Stat. Soc. Series B Stat. Methodol.* **54**, 541–551 (1992).
26. Hande, K. R. Etoposide: four decades of development of a topoisomerase II inhibitor. *Eur. J. Cancer* **34**, 1514–1521 (1998).
27. Sakaue-Sawano, A., Kobayashi, T., Ohtawa, K. & Miyawaki, A. Drug-induced cell cycle modulation leading to cell-cycle arrest, nuclear mis-segregation, or endoreplication. *BMC Cell Biol.* **12**, 2 (2011).
28. Kastan, M. B., Onyekwere, O., Sidransky, D., Vogelstein, B. & Craig, R. W. Participation of p53 protein in the cellular response to DNA damage. *Cancer Res.* **51**, 6304–6311 (1991).
29. Zamble, D. B., Jacks, T. & Lippard, S. J. p53-Dependent and -independent responses to cisplatin in mouse testicular teratocarcinoma cells. *Proc. Natl. Acad. Sci. U. S. A.* **95**, 6163–6168 (1998).
30. Passalaris, T. M., Benanti, J. A., Gewin, L., Kiyono, T. & Galloway, D. A. The G(2) checkpoint is maintained by redundant pathways. *Mol. Cell. Biol.* **19**, 5872–5881 (1999).
31. Clifford, B., Beljin, M., Stark, G. R. & Taylor, W. R. G2 arrest in response to topoisomerase II inhibitors: the role of p53. *Cancer Res.* **63**, 4074–4081 (2003).
32. Bunz, F. *et al.* Requirement for p53 and p21 to sustain G2 arrest after DNA damage. *Science* **282**, 1497–1501 (1998).
33. Taylor, W. R. & Stark, G. R. Regulation of the G2/M transition by p53. *Oncogene* **20**, 1803–1815 (2001).
34. Zhang, R. *et al.* PTEN enhances G2/M arrest in etoposide-treated MCF-7 cells through activation of the ATM pathway. *Oncol. Rep.* **35**, 2707–2714 (2016).
35. Cliby, W. A. *et al.* Overexpression of a kinase-inactive ATR protein causes sensitivity to DNA-damaging agents and defects in cell cycle checkpoints. *EMBO J.* **17**, 159–169 (1998).
36. Bartek, J. & Lukas, J. Chk1 and Chk2 kinases in checkpoint control and cancer. *Cancer Cell* **3**, 421–429 (2003).
37. Siddik, Z. H. Cisplatin: mode of cytotoxic action and molecular basis of resistance. *Oncogene* **22**, 7265–7279 (2003).
38. Dasari, S. & Tchounwou, P. B. Cisplatin in cancer therapy: molecular mechanisms of action. *Eur. J. Pharmacol.* **740**, 364–378 (2014).
39. Pabla, N., Huang, S., Mi, Q.-S., Daniel, R. & Dong, Z. ATR-Chk2 signaling in p53 activation and DNA damage response during cisplatin-induced apoptosis. *J. Biol. Chem.* **283**, 6572–6583 (2008).
40. Patil, M., Pabla, N. & Dong, Z. Checkpoint kinase 1 in DNA damage response and cell cycle regulation. *Cell. Mol. Life Sci.* **70**, 4009–4021 (2013).
41. Sun, B., Ross, S. M., Rowley, S., Adeleye, Y. & Clewell, R. A. Contribution of ATM and ATR kinase pathways to p53-mediated response in etoposide and methyl methanesulfonate induced DNA damage. *Environ. Mol. Mutagen.* **58**, 72–83 (2017).
42. Puig, P.-E. *et al.* Tumor cells can escape DNA-damaging cisplatin through DNA endoreduplication and reversible polyploidy. *Cell Biol. Int.* **32**, 1031–1043 (2008).
43. Cantero, G., Pastor, N., Mateos, S., Campanella, C. & Cortés, F. Cisplatin-induced endoreduplication in CHO cells: DNA damage and inhibition of topoisomerase II. *Mutat. Res.* **599**, 160–166 (2006).
44. Swift, L. H. & Golsteyn, R. M. Cytotoxic amounts of cisplatin induce either checkpoint adaptation or apoptosis in a concentration-dependent manner in cancer cells. *Biol. Cell* **108**, 127–148 (2016).
45. Kubara, P. M. *et al.* Human cells enter mitosis with damaged DNA after treatment with pharmacological concentrations of genotoxic agents. *Biochem. J* **446**, 373–381 (2012).
46. Syljuåsen, R. G. Checkpoint adaptation in human cells. *Oncogene* **26**, 5833–5839 (2007).

47. Swift, L. H. & Golsteyn, R. M. Genotoxic anti-cancer agents and their relationship to DNA damage, mitosis, and checkpoint adaptation in proliferating cancer cells. *Int. J. Mol. Sci.* **15**, 3403–3431 (2014).
48. Kratz, A. *et al.* A multi-scale map of protein assemblies in the DNA damage response. *Cell Syst* **14**, 447-463.e8 (2023).
49. Hiemstra, S. *et al.* Comprehensive Landscape of Nrf2 and p53 Pathway Activation Dynamics by Oxidative Stress and DNA Damage. *Chem. Res. Toxicol.* **30**, 923–933 (2017).
50. Márton, M., Tihanyi, N., Gyulavári, P., Bánhegyi, G. & Kapuy, O. NRF2-regulated cell cycle arrest at early stage of oxidative stress response mechanism. *PLoS One* **13**, e0207949 (2018).
51. Overton, K. W., Spencer, S. L., Noderer, W. L., Meyer, T. & Wang, C. L. Basal p21 controls population heterogeneity in cycling and quiescent cell cycle states. *Proc. Natl. Acad. Sci. U. S. A.* **111**, E4386-93 (2014).
52. Hsu, C.-H., Altschuler, S. J. & Wu, L. F. Patterns of Early p21 Dynamics Determine Proliferation-Senescence Cell Fate after Chemotherapy. *Cell* **178**, 361-373.e12 (2019).
53. Sheng, C. *et al.* PCNA-Mediated Degradation of p21 Coordinates the DNA Damage Response and Cell Cycle Regulation in Individual Cells. *Cell Rep.* **27**, 48-58.e7 (2019).
54. Chen, S.-H. & Chang, J.-Y. New Insights into Mechanisms of Cisplatin Resistance: From Tumor Cell to Microenvironment. *Int. J. Mol. Sci.* **20**, (2019).
55. Martz, E. & Steinberg, M. S. The role of cell-cell contact in “contact” inhibition of cell division: a review and new evidence. *J. Cell. Physiol.* **79**, 189–210 (1972).
56. Wilkinson, D. J. Stochastic modelling for quantitative description of heterogeneous biological systems. *Nat. Rev. Genet.* **10**, 122–133 (2009).

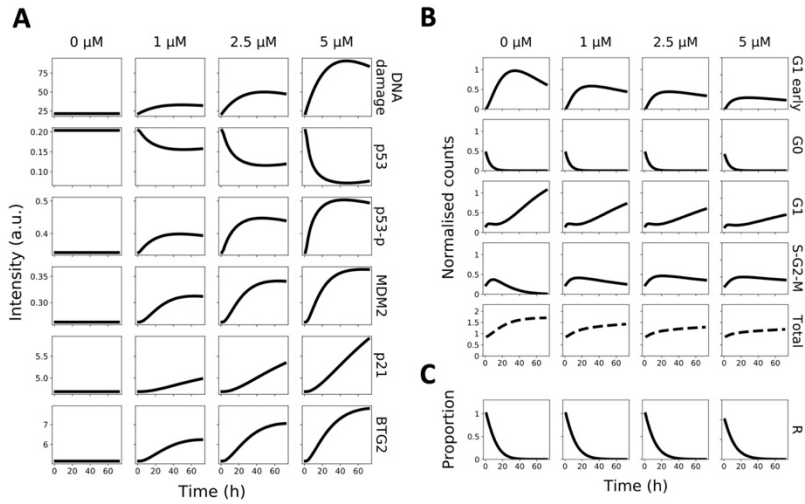
## Supplementary Figures



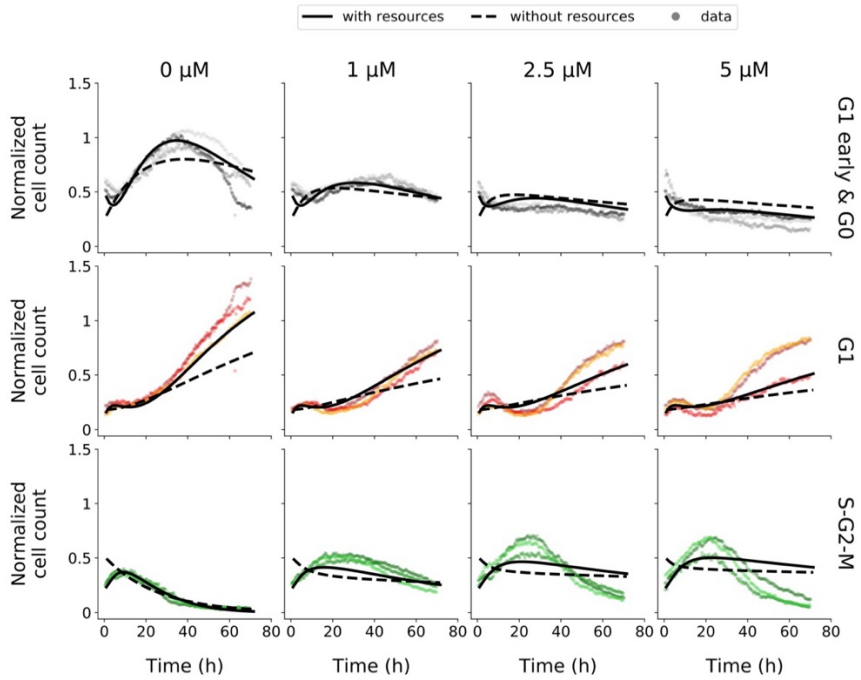
**Supplementary Figure 1. Quantification and classification of cell cycle phases based on Cdt1-RFP and Geminin-GFP intensities.** (A-B) Example distribution of Cdt1 and Geminin expression in all cells from one image set, i.e., all time points at one position in a well, before (A) and after (B) spectral leakage correction. (C) Example distribution of Cdt1-RFP and Geminin-GFP intensities at 0, 24, 48 and 72 h after exposure in 5  $\mu$ M cisplatin condition. The horizontal grey dashed line indicates the 5% threshold, below which Cdt1 and Geminin expression is low and classified as colorless. (D) Example image of Cdt1 and Geminin expression at 24 h after 5  $\mu$ M cisplatin exposure. The dashed lines represent the utilized 5% expression thresholds, resulting in the classification of cell cycle phases as indicated by colors. In A-D each dot represents one cell.



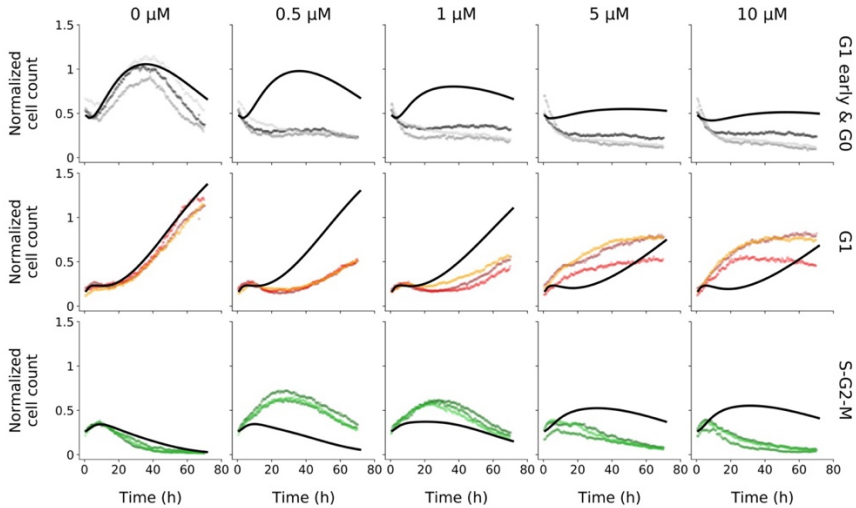
**Supplementary Figure 2. Concentration-dependent reduction in the total HepG2 cell numbers over time due to cisplatin exposure.** The percentage of cells relative to initial cell number is shown over time in control conditions (0  $\mu\text{M}$ ) and after different cisplatin exposure concentrations.



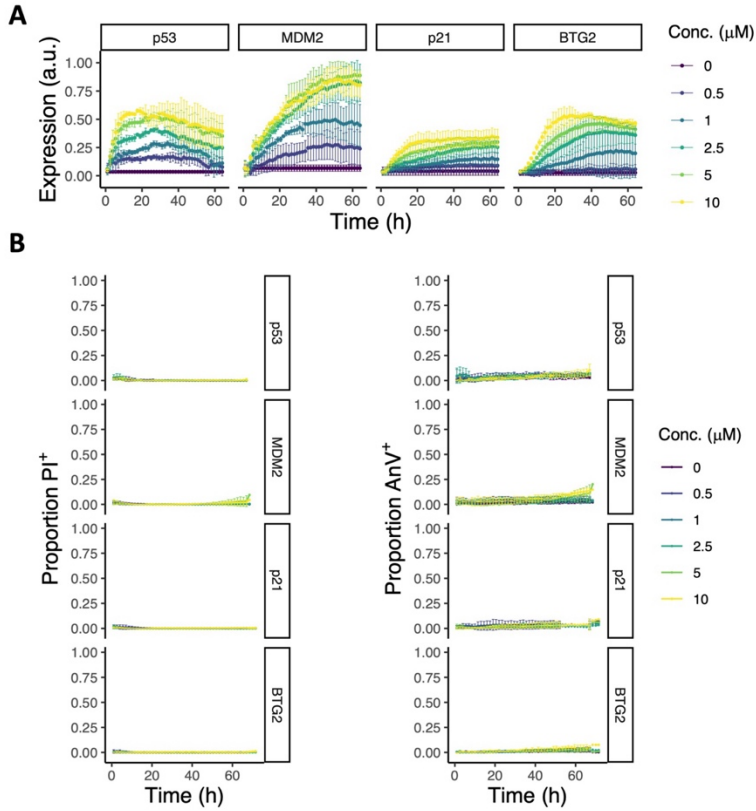
**Supplementary Figure 3. Inner states of the model simulation after 0, 1, 2.5 and 5  $\mu\text{M}$  cisplatin exposure.** (A) Simulation of DNA damage and relevant proteins in the p53 signaling model. (B) Simulations of the normalized number of cells in the distinct cell cycle phases. Initially the normalized cell numbers add up to unity. (C) Model simulation of the proportion of resources available over time relative to the initial amount (set to 1).



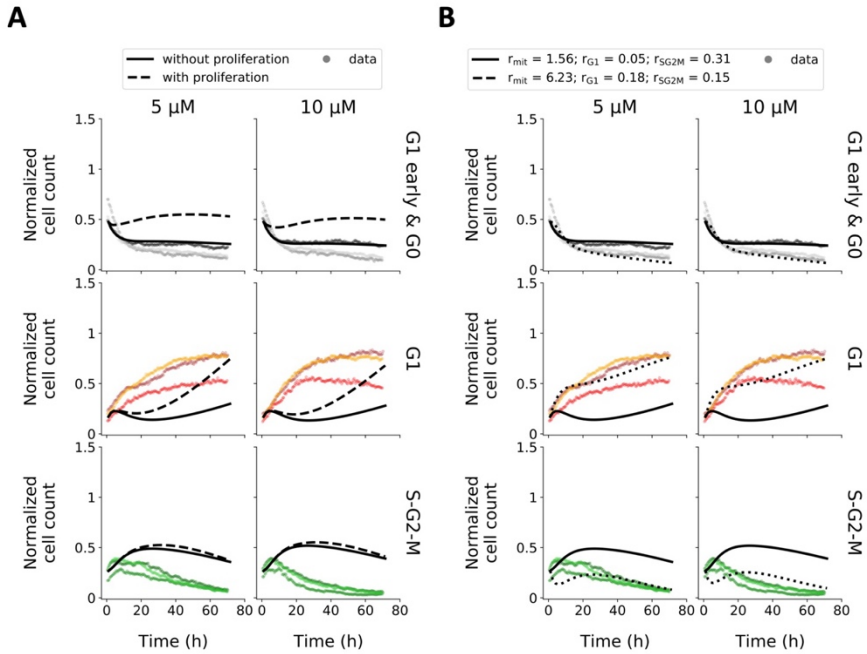
**Supplementary Figure 4. Effect of the presence or absence of resources in the model on the model fit.** Data points of different colors represent the three independent biological replicates per cell cycle phase class. Lines represent model simulations with (M1, solid line) and without (M2, dashed line) the inclusion of resources.



**Supplementary Figure 5. Simulation of the cell cycle model in control situation for low and high etoposide exposure scenarios.** Data points of different colors represent the three independent biological replicates per cell cycle phase class. Lines represent model simulations of the cell cycle model with  $k$ -parameters fitted to correctly model the control situation (M7). Note that the description of scenarios with etoposide exposure is poor.



**Supplementary Figure 6. Effect of etoposide exposure on protein expression and cell death occurrences.** (A) Normalized protein expression and (B) fraction of PI-positive (left) and AnV-positive (right) cells in control condition (0  $\mu\text{M}$ ) and after exposure to 0.5, 1, 2.5, 5 and 10  $\mu\text{M}$  etoposide for each reporter cell line. Data points show mean  $\pm$  sd of three or four biological replicates.



**Supplementary Figure 7. Modulation of cell cycle transition rates improves description of data by the cell cycle model in high etoposide exposure scenarios.** (A-B) Simulation of the cell cycle model (M7) to the cell cycle data in high (5 and 10 μM) etoposide exposure conditions with cell cycle phase transitions, either with (dashed line) or without cell division (solid line) in (A), and without cell division and with modulation of the three cell cycle transition rates in (B).

## Supplementary Methods

We used the p53 model in published in <sup>1</sup> to simulate the dynamics of p53 and its downstream targets MDM2, p21 and BTG2:

$$S(t) = EC_i \cdot e^{-\tau \cdot t}, \quad S.Eq. 1$$

$$\frac{dDD}{dt} = k_{S_{DD}} - k_{d_{DD}} \cdot DD \cdot P53_p + S, \quad S.Eq. 2$$

$$\frac{dP53}{dt} = k_{S_{p53}} + k_{d_p} \cdot P53_p - k_p \cdot P53 \cdot DD - k_{d_{p53}} \cdot P53 - k_{d_{p53 \text{ mdm2}}} \cdot P53 \cdot MDM2, \quad S.Eq. 3$$

$$\frac{dP53_p}{dt} = k_p \cdot P53 \cdot DD - k_{d_p} \cdot P53_p - k_{d_{p53_p}} \cdot P53_p - k_{d_{p53_p \text{ mdm2}}} \cdot P53_p \cdot MDM2, \quad S.Eq. 4$$

$$\frac{dMDM2}{dt} = k_{S_{mdm2}} + \frac{k_{S_{mdm2 \text{ p53p}}} \cdot P53_p^4}{K_{m_{mdm2}} + P53_p^4} - k_{d_{mdm2}} \cdot MDM2, \quad S.Eq. 5$$

$$\frac{dP21}{dt} = k_{S_{p21}} + \frac{k_{S_{p21 \text{ p53p}}} \cdot P53_p^4}{K_{m_{p21}} + P53_p^4} - k_{d_{p21}} \cdot P21, \text{ and} \quad S.Eq. 6$$

$$\frac{dBTG2}{dt} = k_{S_{btg2}} + \frac{k_{S_{btg2 \text{ p53p}}} \cdot P53_p^4}{K_{m_{btg2}} + P53_p^4} - k_{d_{btg2}} \cdot BTG2. \quad S.Eq. 7$$

## Supplementary Data

**Supplementary Table 1.** Parameter description and estimated values of the p53 signaling model to describe protein expression data after cisplatin exposure, as published in <sup>1</sup> (i.e., parameter values for this submodel are exactly the same as in this publication).

Parameter	Unit	Description	Estimated values
DD <sub>init</sub>	-	initial amount of DNA damage	21.443
P53 <sub>init</sub>	au	initial amount of p53	0.204
P53P <sub>init</sub>	au	initial amount of p53-p	0.342
MDM2 <sub>init</sub>	au	initial amount of MDM2	0.263
P21 <sub>init</sub>	au	initial amount of p21	4.686
BTG2 <sub>init</sub>	au	initial amount of BTG2	5.156
EC <sub>0</sub>	-	effective concentration for control condition (0 μM applied concentration)	0*
EC <sub>1</sub>	-	effective concentration for 1 μM applied concentration	1*
EC <sub>2</sub>	-	effective concentration for 2.5 μM applied concentration	2.520
EC <sub>3</sub>	-	effective concentration for 5 μM applied concentration	6.307
τ	hr <sup>-1</sup>	cisplatin decay rate	0.020
kd <sub>mdm2</sub>	hr <sup>-1</sup>	degradation rate of MDM2	0.082
kd <sub>p21</sub>	hr <sup>-1</sup>	degradation rate of p21	0.003
kd <sub>btg2</sub>	hr <sup>-1</sup>	degradation rate of BTG2	0.047
kd <sub>dd</sub>	au <sup>-1</sup> · hr <sup>-1</sup>	DNA damage repair rate	0.042
k <sub>dp</sub>	hr <sup>-1</sup>	dephosphorylation rate of p53-p	0.410
kd <sub>p53</sub>	hr <sup>-1</sup>	degradation rate of p53	0.047
kd <sub>p53p</sub>	hr <sup>-1</sup>	degradation rate of p53-p	0.0002
kd <sub>p53 mdm2</sub>	au <sup>-1</sup> · hr <sup>-1</sup>	MDM2-dependent degradation rate of p53	0.00002
kd <sub>p53p mdm2</sub>	au <sup>-1</sup> · hr <sup>-1</sup>	MDM2-dependent degradation rate of p53-p	0.069
kS <sub>mdm2 p53p</sub>	au · hr <sup>-1</sup>	maximal p53-p-dependent synthesis rate of MDM2	0.033
kS <sub>p21 p53p</sub>	au · hr <sup>-1</sup>	maximal p53-p-dependent synthesis rate of p21	0.171
K <sub>mmdm2</sub>	au	Michaelis-Menten constant for MDM2	0.296
K <sub>mp21</sub>	au	Michaelis-Menten constant for p21	0.741
K <sub>m<sub>btg2</sub></sub>	au	Michaelis-Menten constant for BTG2	0.382
kS <sub>btg2 p53p</sub>	au · hr <sup>-1</sup>	maximal p53-p-dependent synthesis rate of BTG2	0.370
kS <sub>dd</sub>	hr <sup>-1</sup>	rate of DNA damage infliction	0.305
k <sub>p</sub>	hr <sup>-1</sup>	phosphorylation rate of p53	0.033
ks <sub>p53</sub>	hr <sup>-1</sup>	synthesis rate of p53	0.016
kS <sub>mdm2</sub>	hr <sup>-1</sup>	synthesis rate of MDM2	0.0003
ks <sub>p21</sub>	hr <sup>-1</sup>	synthesis rate of p21	0.008
ks <sub>btg2</sub>	hr <sup>-1</sup>	synthesis rate of BTG2	0.096
sf <sub>p53</sub>	-	scaling factor for total p53	16.882
sf <sub>mdm2</sub>	-	scaling factor for MDM2	5.390
sf <sub>p21</sub>	-	scaling factor for p21	0.291
sf <sub>btg2</sub>	-	scaling factor for BTG2	0.154
offset <sub>p53</sub>	-	offset for total p53	-9.157
offset <sub>mdm2</sub>	-	offset for MDM2	-1.324
offset <sub>p21</sub>	-	offset for p21	-1.309
offset <sub>btg2</sub>	-	offset for BTG2	-0.783

\* Fixed parameter values

**Supplementary Table 2.** Parameter descriptions and values estimated for the default cell cycle model (M1, M7), the model without resources (M2), the model fitted to the data until 24 h (M3), the model without inhibition of G1 to S-G2-M transition by p21 (M4) or by p21 and BTG2 (M5), the model without mitosis inhibition by BTG2 (M6). Model M1-M6 were fitted to the cisplatin cell cycle progression data and model M7 to etoposide cell cycle progression data.

Parameter	Unit	Description	Value in M1	Value in M2	Value in M3	Value in M4	Value in M5	Value in M6	Value in M7
$G1_{\text{early, init}}$	-	Initial proportion of cells in early G1	0	0	0.105	0	0	0	0.105*
$G0_{\text{init}}$	-	Initial proportion of cells in G0	0.454	0.281	0.368	0.453	0.453	0.402	0.368*
$G1_{\text{init}}$	-	Initial proportion of cells in G1	0.161	0.183	0.171	0.161	0.162	0.159	0.171*
$SG2M_{\text{init}}$	-	Initial proportion of cells in S-G2-M	0.233	0.495	0.267	0.233	0.232	0.211	0.267*
$R_{\text{init}}$	-	Initial proportion of resources	1*	-	1*	1*	1*	1*	1*
$s$	-	Scaling factor for depletion of resources	0.138	-	0.076	0.149	0.164	0.175	0.076*
$\Gamma_{\text{exit}}$	$h^{-1}$	Rate constant of cell cycle exit into G0 from early G1	0*	0*	0*	0*	0*	0*	0*
$\Gamma_{\text{entry}}$	$h^{-1}$	Rate constant of entry into G1 from G0	0.195	0.002	0.191	0.194	0.190	0.156	0.191*
$\Gamma_{G1}$	$h^{-1}$	Rate constant of transition from early G1 into G1	0.021	0.016	0.030	0.020	0.020	0.024	0.030*
$\Gamma_{SG2M}$	$h^{-1}$	Rate constant of transition from G1 into S-G2-M	1.152	0	0.205	0.295	0.294	0.258	0.205*
$\Gamma_{\text{mit}}$	$h^{-1}$	Rate constant of mitosis	0.144	0.512	1.039	0.136	0.123	2.942	1.039*
$k_1$	-	Contribution factor of BTG2 on mitosis rate	72.890	1000	1000	68.623	60.190	0*	2.769
$k_2$	-	Contribution factor of p21 on mitosis rate	0	0	0	0*	0*	1000	203.11
$k_3$	-	Contribution factor of BTG2 on G1 progression rate into S-G2-M	0	$1 \cdot 10^{-4}$	0	2.547	0*	0*	0
$k_4$	-	Contribution factor of p21 on G1 progression rate into S-G2-M	55.901	1000	0	0*	0*	0	0

\* Fixed parameter values

**Supplementary Table 3.** Parameter description and estimated values of the p53 signaling model to describe protein expression data after etoposide exposure.

Parameter	Unit	Description	Estimated values
$DD_{init}$	-	initial amount of DNA damage	0.986
$P53_{init}$	au	initial amount of p53	0.887
$P53P_{init}$	au	initial amount of p53-p	0.132
$MDM2_{init}$	au	initial amount of MDM2	0.832
$P21_{init}$	au	initial amount of p21	3.154
$BTG2_{init}$	au	initial amount of BTG2	2.339
$EC_0$	-	effective concentration for control condition (0 $\mu$ M applied concentration)	0*
$EC_1$	-	effective concentration for 0.5 $\mu$ M applied concentration	0.5*
$EC_2$	-	effective concentration for 1 $\mu$ M applied concentration	1.117
$EC_3$	-	effective concentration for 5 $\mu$ M applied concentration	4.099
$EC_4$	-	effective concentration for 10 $\mu$ M applied concentration	6.906
$\tau$	hr <sup>-1</sup>	etoposide decay rate	0.080
$kd_{mdm2}$	hr <sup>-1</sup>	degradation rate of MDM2	0.050
$kd_{p21}$	hr <sup>-1</sup>	degradation rate of p21	0.096
$kd_{btg2}$	hr <sup>-1</sup>	degradation rate of BTG2	0.113
$kd_{dd}$	au <sup>-1</sup> · hr <sup>-1</sup>	DNA damage repair rate	0.019
$k_{dp}$	hr <sup>-1</sup>	dephosphorylation rate of p53-p	81.459
$kd_{p53}$	hr <sup>-1</sup>	degradation rate of p53	7.431
$kd_{p53p}$	hr <sup>-1</sup>	degradation rate of p53-p	4.504
$kd_{p53\ mdm2}$	au <sup>-1</sup> · hr <sup>-1</sup>	MDM2-dependent degradation rate of p53	0.034
$kd_{p53p\ mdm2}$	au <sup>-1</sup> · hr <sup>-1</sup>	MDM2-dependent degradation rate of p53-p	0.012
$ks_{mdm2\ p53p}$	au · hr <sup>-1</sup>	maximal p53-p-dependent synthesis rate of MDM2	0.014
$ks_{p21\ p53p}$	au · hr <sup>-1</sup>	maximal p53-p-dependent synthesis rate of p21	0.159
$K_{m_{mdm2}}$	au	Michaelis-Menten constant for MDM2	0.544
$K_{m_{p21}}$	au	Michaelis-Menten constant for p21	0.772
$K_{m_{btg2}}$	au	Michaelis-Menten constant for BTG2	0.828
$ks_{btg2\ p53p}$	au · hr <sup>-1</sup>	maximal p53-p-dependent synthesis rate of BTG2	0.246
$ks_{dd}$	hr <sup>-1</sup>	rate of DNA damage infliction	0.002
$k_p$	hr <sup>-1</sup>	phosphorylation rate of p53	12.992
$ks_{p53}$	hr <sup>-1</sup>	synthesis rate of p53	7.210
$ks_{mdm2}$	hr <sup>-1</sup>	synthesis rate of MDM2	0.042
$ks_{p21}$	hr <sup>-1</sup>	synthesis rate of p21	0.302
$ks_{btg2}$	hr <sup>-1</sup>	synthesis rate of BTG2	0.264
$sf_{p53}$	-	scaling factor for total p53	1.316
$sf_{mdm2}$	-	scaling factor for MDM2	3.129
$sf_{p21}$	-	scaling factor for p21	0.203
$sf_{btg2}$	-	scaling factor for BTG2	0.286
$offset_{p53}$	-	offset for total p53	-1.322
$offset_{mdm2}$	-	offset for MDM2	-2.502
$offset_{p21}$	-	offset for p21	-0.590
$offset_{btg2}$	-	offset for BTG2	-0.643

\* Fixed parameter values

## References

- Heldring, M. M., Shaw, A. H. & Beltman, J. B. Unraveling the effect of intra- and intercellular processes on acetaminophen-induced liver injury. *NPJ Syst Biol Appl* **8**, 27 (2022).

